

# A High-Sensitivity Small-Animal PET Scanner: Development and Initial Performance Measurements

Chien-Min Kao, *Senior Member, IEEE*, Qingguo Xie, *Member, IEEE*, Yun Dong, Lu Wan, and Chin-Tu Chen

**Abstract**—An important challenge in positron emission tomography (PET) is the development of dedicated small-animal PET ( $\mu$ PET) systems having high sensitivity. In this paper, we investigate the use of an opposing pair of large-area detectors having high detection efficiency and moderate depth-of-interaction resolution in a compact scanner geometry for achieving a high system sensitivity. Substantial resolution degradations created by this hardware configuration, on the other hand, are corrected for by applying model-based image reconstruction. We have developed a prototype scanner adopting this design and evaluated its performance properties. Our results show that the prototype can achieve a central sensitivity of  $\sim 28.2\%$  when using an energy window (EW) of 250–750 keV and a coincidence time window (CW) of 10 ns. When decreasing the EW to 400–750 keV, the central sensitivity still remains high at  $\sim 14.4\%$ . Over the typical ranges of radioactivity used in PET rodent imaging with [ $^{18}\text{F}$ ]fluorodeoxyglucose (FDG), the prototype provides noise-equivalent count rates (NECRs) that are considerably higher than other  $\mu$ PET systems. For a mouse/rat-sized cylinder, we obtain a peak NECR of  $\sim 1.86/1.2$  Mcps at  $\sim 32/40$  MBq when using a 250/350–750 keV EW and a 6 ns CW. Using a resolution phantom, we obtain an average FWHM (full width at the half-maximum) of 1.79 mm for 1.35 mm-diameter rod sources when the axis of the phantom is vertical to the detectors of the prototype. This is consistent with the 1.2 mm FWHM image resolution previously obtained by using simulation data. The prototype also generates FDG rat images having good visual quality.

**Index Terms**—High-sensitivity PET, positron emission tomography (PET), small-animal PET.

## I. INTRODUCTION

AS positron emission tomography (PET) finds wider use in clinic and research, there arises the need for higher standards on its imaging performance and, at the same time, growing pressure for improving the cost effectiveness of the instrument. To date, PET image resolution has been significantly improved to reach the sub-millimeter level, mostly through advances made to detector technology [1]–[6]. In contrast, the sensitivity of current clinical and small-animal PET ( $\mu$ PET) systems remains low, typically below 5% [5]–[7]. The needs for high sensitivity in PET imaging are not difficult to observe. When using the same amount of radioactivity and imaging time, more sensitive PET systems can generate images having higher

signal-to-noise ratios (SNRs) for improving the detection of abnormalities/changes and the accuracy in quantification [5], [6]. Conversely, to achieve a certain image SNR more sensitive PET systems allow the use of lower radioactivities for reducing the radiation dose to subject, or the use of shorter imaging time for increasing the imaging throughput or improving the temporal resolution in dynamic studies. Also, many applications critically require high sensitivity because the signals of concern are inherently limited in strength. For example, the signal in neuroreceptor imaging can be limited by the number of binding sites available, as well as by the specificity and affinity of the radio-tracers [8]. Similarly, the number of foreign cells that can be used in cell-trafficking studies can be limited and long tracking time to follow the cells is often necessary [9].

The advent of  $\mu$ PET imaging has elevated the concern for insufficient sensitivity. To maintain the quantitative accuracy per image voxel under similar imaging conditions, the volumetric resolution and sensitivity need to be improved by the same amount. In view of this, investigators have already noted that the sensitivity of the current  $\mu$ PET systems is significantly lacking with respect to that of the clinical PET systems [5]–[7]. This inadequate sensitivity can be compensated for to some extent by use of long imaging times and/or high radioactivity concentrations. However, at present the level of radioactivity used in typical  $\mu$ PET imaging protocols can yield a radiation dose ten times that in clinical PET imaging, giving rise to serious concerns for the presence of non-trivial radiobiological effects in current  $\mu$ PET studies [6], [10].

Developing affordable high-sensitivity (HS)  $\mu$ PET systems is therefore of great significance. The task also presents substantial challenges. Efforts are being taken to address the need for HS  $\mu$ PET imaging. For example, the Siemens Inveon system has recently been reported to achieve a central sensitivity of 9.3% [11]. We have also previously reported a promising system design approach for addressing challenges in developing HS  $\mu$ PET system [12]. We have examined the use of an opposing pair of large-area detectors having high detection efficiency and moderate depth-of-interaction (DOI) resolution in a compact scanner geometry for achieving a high system sensitivity. Substantial resolution degradations created by the hardware configuration, on the other hand, are corrected for by applying model-based image reconstruction. In this paper, we present a prototype adopting this design and report our initial measurements of its performance properties.

## II. DESIGN CONSIDERATIONS

The task of increasing PET system sensitivity appears simple: to obtain a high geometric efficiency (GE) for intercepting most gamma-ray photons originating inside the imaging volume and

Manuscript received August 12, 2008; revised January 14, 2009 and May 07, 2009. Current version published October 07, 2009.

C.-M. Kao and C.-T. Chen are with the Department of Radiology, The University of Chicago, Chicago, Illinois, USA (e-mail: c-kao@uchicago.edu; c-chen@uchicago.edu).

Q. Xie and L. Wan are with the Biomedical Engineering Department, Huazhong University of Science and Technology, Wuhan, Hubei, China (e-mail: qgxie@ieee.org; loowan2006@gmail.com).

Y. Dong is with the Department of Biomedical Engineering, Illinois Institute of Technology, Chicago, Illinois, USA (e-mail: dongyun@iit.edu).

Digital Object Identifier 10.1109/TNS.2009.2026647

a high detection efficiency (DE) for the detectors so that most intercepted photons are registered. This, however, turns out to be a non-trivial task.

#### A. Considerations for Increasing GE and DE

To obtain high GEs, one needs large detection solid-angles (DSAs) and dense packing of the detectors. For yielding large DSAs, a compact scanner having a large axial FOV (AFOV) is favorable. Compact geometry is interesting due to cost effectiveness: with a more compact geometry—i.e., a geometry that places detectors closer to the activities—a smaller detection surface area (hence less detector material) is required to cover a given DSA. A large AFOV not only increases the DSA, it also reduces the number of bed positions needed for imaging a subject. Also, the sensitivity of a PET scanner decreases from a maximum at the center—which is the *central sensitivity*—to zero at the edges of the AFOV. Therefore, given two scanners having the same central sensitivity the longer one will have a higher sensitivity to a subject (called *subject sensitivity* below) than the shorter one because the average sensitivity to the subject volume is higher with the former.<sup>1</sup> Therefore, the gain in subject sensitivity provided by a larger-AFOV scanner over a smaller-AFOV scanner can be considerably higher than suggested by the difference in their reported central sensitivities.

To obtain high DEs, the detectors shall employ thick and dense scintillators and contain small detection inactive volumes. For  $\mu$ PET imaging, the detector also needs to use narrow crystals for providing high intrinsic spatial resolution. A 1.2 mm image resolution is useful for many applications in  $\mu$ PET imaging, but a higher resolution is welcome. Based on our empirical observations with existing  $\mu$ PET systems [3], [6], [13], this resolution would require the use of  $\sim 1.2$  mm wide (or narrower) crystals. Using narrow and thick detectors in a compact geometry is the recipe for producing pronounced DOI blurring that will severely degrade the image resolution. The negative impact of DOI blurring to PET image quality has been widely documented [5], [6] and the development of DOI detectors is an important and active field of research [14]–[24]. Ideally, the DOI resolution shall be comparable with the crystal width so that the crystal's apparent aperture does not significantly change as the gamma-ray incident angle varies.

The above considerations suggest that an HS  $\mu$ PET system desires a compact and long geometry and shall employ detectors that have high detection efficiency, high intrinsic resolution and high DOI resolution. On the other hand, the cost of the system also needs to remain attractive to biomedical research laboratories. Currently, mature technologies for producing high-performance PET detectors—e.g., that can provide 2–3 attenuation lengths (or longer) for 511 keV gamma rays, 1.2 mm intrinsic resolution (or better), and  $\sim 1$ –3 mm DOI resolution—in large quantity and at low cost are not available. It is widely shared among PET investigators that, for developing HS  $\mu$ PET systems with adequate FOV, at the present time one shall focus on substantially improving the performance and cost effectiveness of the detector technology.

<sup>1</sup>Similarly, given two scanners having the same central sensitivity the longer one will produce a more uniform noise distribution within a subject because sensitivity variations within the subject volume are smaller.

We note that large-area detector panels (called *detector plates* below) are of interest with respect to increasing the GE and DE. For covering a given detection surface, the use of detector plates can reduce detector gaps and yield dense packing. In addition, cost-effective designs have been proposed for building detector plates (e.g., the quadrant-sharing configuration [25] and the Anger-logic detectors [26]); many new high-performance detector technologies under examination naturally lead to the plate geometry [14], [27]–[29]; and the use of detector plates naturally yields an extended scanner AFOV.

#### B. An Integrative Design Strategy

The above discussion indicates the fundamental importance of detector technology in developing PET systems, with the observation that the performance limitations of available detector technologies have hindered the current development of HS  $\mu$ PET systems. The discussion, however, has neglected the well-known ability of model-based reconstruction methods—i.e., reconstruction methods that employ accurate models of the physical and statistical properties of the detection responses of the system—in compensating for various image-quality degrading factors in the detection process [30], [31]. As PET image quality is affected by both the hardware (detectors and scanner geometry) and software (reconstruction) features of the system, the concept of integrative design strategy naturally arises: one shall create synergistic combinations for the hardware and software components to obtain PET system designs that can meet system performance targets with relaxed hardware performance requirements, improved cost effectiveness, or other practical benefits.

We have investigated the use of this integrative design strategy for mitigating the hardware challenges facing the current development of HS  $\mu$ PET systems. By using computer simulations, we have previously demonstrated the possibility to build an HS  $\mu$ PET system by using the off-the-shelf, HRRT (High Resolution Research Tomograph) detector technology [32]–[34]. Below in Section III, we will present a prototype that adopts the proposed design. As it will be made clear, the design of the prototype relies on the hardware features for achieving a high system sensitivity and a large imaging volume, and on the software features for producing adequate spatial resolution for  $\mu$ PET imaging. To avoid distractions, however, several important integrative design considerations for the prototype are given later in the Appendix.

### III. THE PROTOTYPE

#### A. Hardware Configuration

We sought a mature, off-the-shelf detector technology for developing the proposed HS  $\mu$ PET system and identified the HRRT detector technology as particularly promising [35]–[37]. Fig. 1 shows our stationary, table-top prototype. The HRRT detector head has a detection active area of  $\sim 25 \times 17$  cm<sup>2</sup>. It contains a  $9 \times 13$  array of crystal blocks, coupled to a  $10 \times 14$  array of photomultiplier tubes in a cost-effective quadrant-sharing configuration. An individual crystal block contains  $8 \times 8$  double-layered LSO/LYSO detection elements, each of which is  $2.1 \times 2.1 \times 20$  mm<sup>3</sup> in size (a crystal segment is 10



Fig. 1. Our stationary, table-top prototype consists of two HRRT detectors in a compact geometry for yielding a high system sensitivity. The HRRT detector has a detection active area of  $\sim 25 \times 17 \text{ cm}^2$  and the detector spacing as shown is  $\sim 5 \text{ cm}$ . The hardware configuration will result in substantial resolution degradations. These degradations are corrected for by using a model-based reconstruction method.

mm long). The crystal pitch is  $\sim 2.43 \text{ mm}$ . The scintillation materials LSO and LYSO offer a good stopping power for 511 keV gamma rays, high light yields, and short scintillation decay constants. The difference in the LSO and LYSO decay constants allows the electronics to determine the layer in which a detection event occurs, yielding a DOI resolution of  $\sim 10 \text{ mm}$ . The HRRT electronics allow users to apply a wide range of energy windows (EWs) and offer four coincidence time windows (CWs) of 2 ns, 6 ns, 10 ns and 22 ns. List-mode data are generated. The prototype is stationary and assumes a 5 cm detector spacing. The entire volume between the two detectors is allowed for imaging, creating a  $25 \times 17 \times 5 \text{ cm}^3$  detection-sensitive volume (DSV).

Based on the HRRT detector size and the detector spacing, the prototype provides a GE of  $\sim 80\%$  for a point source at its center. Based on the HRRT's packing fraction and its scintillator materials and thickness, its DE for 511 keV photon is  $\sim 61\%$  (assuming normally incident gamma rays and that all interacting events are detected). Therefore, we obtain a first-order estimate of  $\sim 29.8\%$  for the central sensitivity of the prototype. We note that the above DE estimate ignores the effect of the EW in relation to the detector energy resolution (including this will decrease the DE). It also neglects that with the compact geometry most gamma rays enter the detectors obliquely (including this will increase the DE).

On the other hand, it is observed that the HRRT system, which employs eight HRRT detectors in an octagonal geometry for imaging human brains, has an image resolution slightly worse than 2 mm [36], [37]. The prototype's compact geometry will create substantial DOI blurring to degrade the image resolution further from this level. Consequently, without compensating for resolution degradation the prototype will not be able to provide an adequate resolution for  $\mu\text{PET}$  imaging.

### B. Reconstruction Method

The 2.4 mm crystal pitch of the HRRT detector suggests an intrinsic detector resolution of  $\sim 1.2 \text{ mm}$  [38], [39]. Therefore, we chose a target image resolution of 1.2 mm for the prototype (see Appendix) and employed  $0.6 \times 0.6 \times 0.5 \text{ mm}^3$  image voxels to support this resolution. To maximally retain data information, no data rebinning was applied for reducing the amount of data before reconstruction. The spatial responses of the prototype with respect to the selected image voxels were calculated for

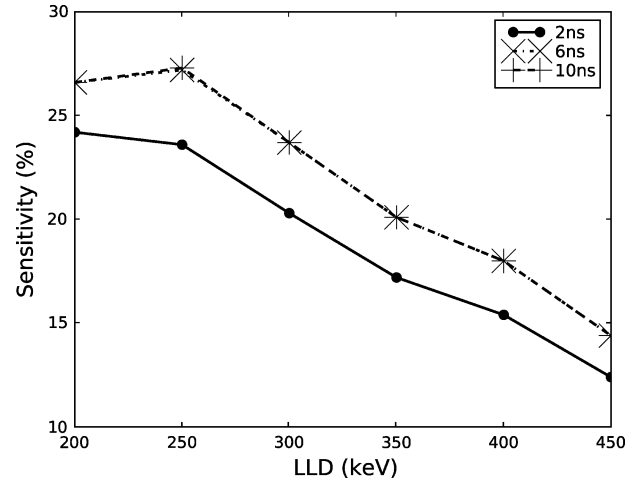


Fig. 2. The central sensitivity of the prototype estimated by using MC simulation. A 20% energy resolution and a 3 ns coincidence timing resolution are assumed. The horizontal axis is the lower-level discriminator (LLD) setting of the EW, with the upper-level discriminator fixed at 750 keV. The vertical axis is the central sensitivity in percentage. Three CWs, including 2 ns, 6 ns and 10 ns, are considered. The results obtained by using the 6 ns and 10 ns CWs are essentially identical.

individual lines of response (LORs) of the prototype. An LOR-based ordered-subset expectation-maximization (OSEM) algorithm then employed these pre-calculated responses for reconstruction. A significant challenge in implementing this model-based OSEM algorithm is related to the tremendous dimension of the resulting system matrix (i.e., the matrix that describes the scanner's sensitivity to individual image voxels at individual LORs). Since the HRRT detector contains two layers of  $104 \times 72$  crystals, our prototype contains more than  $10^8$  LORs. With the selected voxel size, the DSV of the prototype contains more than  $10^7$  voxels. The resulting system matrix is thus larger than  $10^8 \times 10^7$ !

We have previously reported that the dual-head geometry of the prototype has substantial symmetries with respect to the selected image voxels [32]–[34]. By exploiting these symmetries, the number of LORs that need to be considered for calculating the system matrix can be greatly reduced, therefore enabling one to calculate the system matrix by MC simulation and overcome the difficulty in storing the matrix. By using simulation data, we have shown the following for the prototype in [32]–[34]. When using a system matrix that models the LOR responses by line integrals in reconstruction, we obtain an image resolution of  $\sim (1.8 \text{ mm})^2$  on planes parallel to the detectors but worse than 3.2 mm in the direction vertical to the detectors. In addition, the resolution shows considerable variations over the DSV of the prototype. In contrast, after employing the MC-generated system matrix in reconstruction an isotropic image resolution of  $\sim 1.2 \text{ mm}$  is obtained and the resolution shows small variations over the DSV. Furthermore, no noticeable image artifacts are observed over the DSV. When applied to simulated noisy data, using the MC-generated system matrix in reconstruction also improves the statistical quality of the image.

Currently, our OSEM algorithm considers only the measurements generated by the front LSO layers. We are extending the algorithm to include both crystal layers.

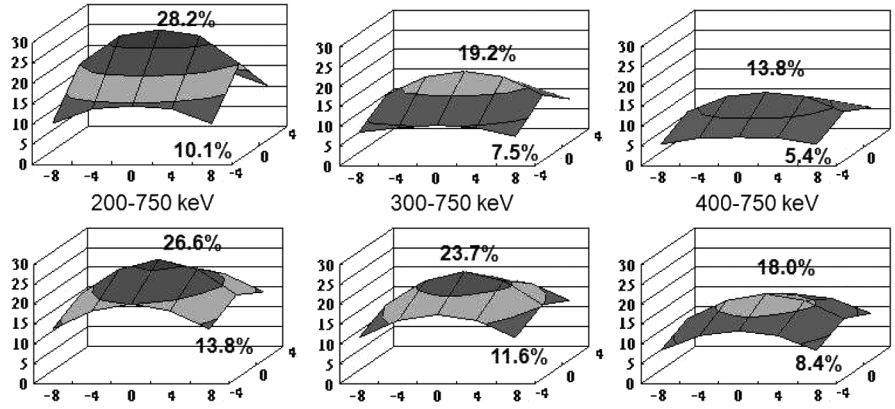


Fig. 3. Sensitivity of the prototype to a  $16 \times 8 \text{ cm}^2$  area on the midplane between the detectors at three EWs and with a 10 ns CW. Top row: measured results by using a small source filled with FDG. Bottom row: Monte Carlo simulation results.

TABLE I  
SCATTER FRACTIONS OF THE PROTOTYPE ESTIMATED BY USING MONTE CARLO SIMULATION

EW	200-750 keV	250-750 keV	300-750 keV	350-750 keV	400-70 keV	450-750 keV
CW	2ns/6ns/10ns	2ns/6ns/10ns	2ns/6ns/10ns	2ns/6ns/10ns	2ns/6ns/10ns	2ns/6ns/10ns
mouse	15.0%/15.2%/15.3%	13.3%/13.4%/13.3%	11.8%/11.7%/11.7%	9.6%/9.7%/9.7%	7.3%/7.2%/7.3%	4.7%/4.7%/4.8%
rat	26.0%/26.4%/26.3%	23.4%/23.5%/23.6%	20.7%/20.6%/20.7%	17.0%/17.0%/17.1%	12.7%/12.7%/12.7%	8.3%/8.3%/8.2%

#### IV. PERFORMANCE EVALUATIONS

##### A. Sensitivity

By using a Ge-68 rod source, we measured the average energy and coincidence timing resolutions of our HRRT detectors to be about 20% at 511 keV and 3 ns FWHM (full width at the half-maximum), respectively. These values are consistent with the results reported by others [36], [37]. We employed the public-domain GATE package to model by MC simulation the responses of the prototype with these average energy and timing resolutions. Fig. 2 shows the resulting central sensitivity obtained for various EWs and three CWs. We observe little difference between the 6 ns- and 10 ns-CW results, and the highest sensitivity is  $\sim 27\%$  (using the 250–750 keV EW). Fig. 3 shows the sensitivity of the prototype to a  $16 \times 8 \text{ cm}^2$  area on the midplane between the detectors, obtained by MC simulation and measurements with FDG ([ $^{18}\text{F}$ ]fluorodeoxyglucose). For the measured results, the branching fraction of the F-18 (0.967) and the background event rates due to the natural radioactivity of Lu-176 in LSO and LYSO were corrected for. These background event rates were obtained for specific EWs and CWs by performing 5-minute scans with no radioactivity inside the FOV. As expected, the sensitivity over the midplane decreases when moving away from the center and when reducing the EW. With the 200–750 keV EW, the measured sensitivity stays above 10% for the entire  $16 \times 8 \text{ cm}^2$  area examined. When using a narrower 400–750 keV EW, the sensitivity over the same area is still above 5.4%. When using the 200–750 keV EW, a central sensitivity of  $\sim 28.2\%$  is measured, slightly higher than the  $\sim 26.6\%$  value obtained by MC simulation. Also, the measured sensitivity decreases faster than does the simulation result when moving away from the center and when reducing the EW. We note that the HRRT detectors showed considerable variations in the energy and timing resolutions across detection channels. Such variations were not included in simulation and might have

contributed to the observed differences between the measured and simulation results.

##### B. Noise-Equivalent Count Rates (NECRs)

We measured the NECR curves for mouse- and rat-sized cylinders by using various EWs and CWs. The mouse-sized cylinder was 2.7 cm in diameter and 8 cm in length, yielding a volume of  $45 \text{ cm}^3$ . The rat-sized cylinder was 4.6 cm in diameter and 13.5 cm in length, yielding a volume of  $220 \text{ cm}^3$ . The cylinders were filled with  $\sim 185 \text{ MBq}$  ( $\sim 5 \text{ mCi}$ ) FDG and the prompt ( $P$ ) and delayed ( $D$ ) event rates were acquired for at least ten half-lives of the FDG. Table I shows the scatter fractions (SFs) of the prototype estimated for various EWs and CWs by using MC simulation. These SFs were employed to calculate the NECRs by use of the following formula:

$$\text{NECR} = \frac{(P - D)^2(1 - \text{SF})^2}{P + D}. \quad (1)$$

The branching fraction of F-18 was corrected for, but the background event rates due to the natural radioactivity of Lu-176 in LSO and LYSO were not.

Fig. 4 shows the count-rate curves obtained by using 2 ns and 6 ns CWs. As expected, both the prompt and delayed event rates increased as wider EWs were used. Also, the delayed event rates increased with the CW. The prompt event rates increased substantially when increasing the CW from 2 ns to 6 ns, suggesting a significant increase in the true and scatter event rates as well. In contrast, the difference in the prompt event rates obtained by using 6 ns and 10 ns CWs (results not shown) can be attributed to the difference in the delayed event rates, suggesting small differences in the true and scatter event rates at these two CW settings. This is consistent with the average 3 ns coincidence timing resolution measured for the prototype. Depending on the EW and CW settings, the prompt event rates of the prototype saturate at a total activity of 20–50 MBq (0.54–1.35 mCi).

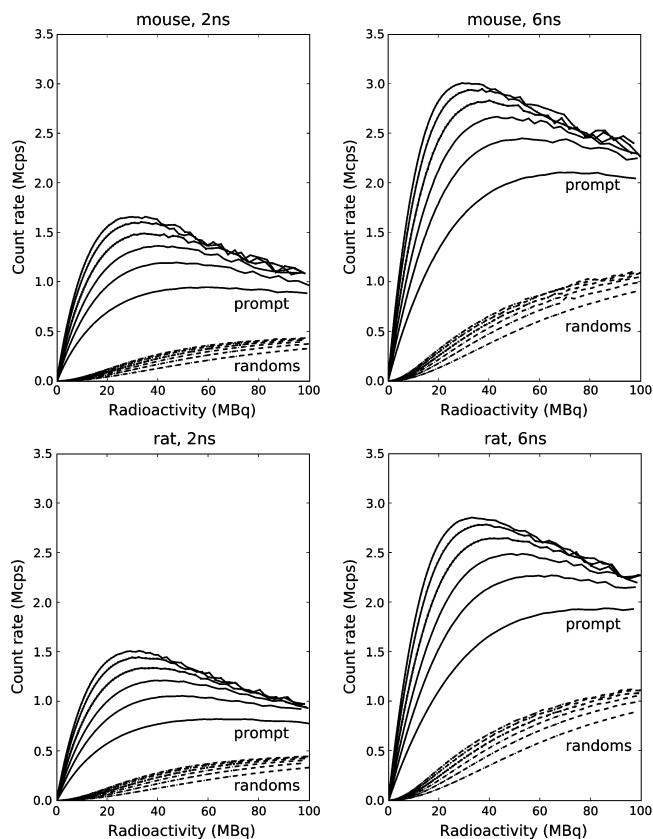


Fig. 4. Measured count-rate curves versus the total radioactivity inside the object obtained for the mouse- and rat-sized cylinders (filled with FDG) by using 2 ns and 6 ns CWs. Each graph contains two groups of curves obtained for the prompt (solid curves) and randoms (dash curves). Each curve group contains results obtained with six EWs having the same upper-level discriminator (ULD) setting of 750 keV. Their lower-level discriminator (LLD) settings are 200 keV, 250 keV, 300 keV, 350 keV, 400 keV, and 450 keV. Within each group, the count rate decreases as the LLD increases.

Fig. 5 shows the NECR curves obtained. It is observed that the use of the 6 ns CW and 250–750 keV EW can yield a good NECR for the typical range of radioactivity used in FDG-PET imaging of mice, yielding a peak NECR value of  $\sim 1.86$  Mcps at  $\sim 32$  MBq total radioactivity. On the other hand, the NECR curve obtained by use of the 6 ns CW and 350–750 keV EW, yielding a peak value of  $\sim 1.2$  Mcps at  $\sim 40$  MBq total radioactivity, is appropriate for the typical range of radioactivity used in FDG-PET imaging of rats. Fig. 6 shows the NECR curves obtained for the prototype when using a 6 ns CW and various EWs, along with the peak locations of the NECR curves reported in the literature for other  $\mu$ PET systems [3], [4], [11], [13], [40]–[56]. The results suggest that the prototype can provide considerably higher NECRs than other existing  $\mu$ PET systems over the typical ranges of radioactivity used in rodent FDG-PET imaging. It is important to emphasize that one must interpret Fig. 6 with great caution: The NECRs reported for various  $\mu$ PET systems are obtained by using different phantom sizes, EWs and CWs; therefore, they shall not be directly compared without reservation.

The noise-equivalent sensitivity (NES) is the slope of the NECR curves at low radioactivity. It provides an estimate of the net sensitivity of a PET scanner with the negative impact

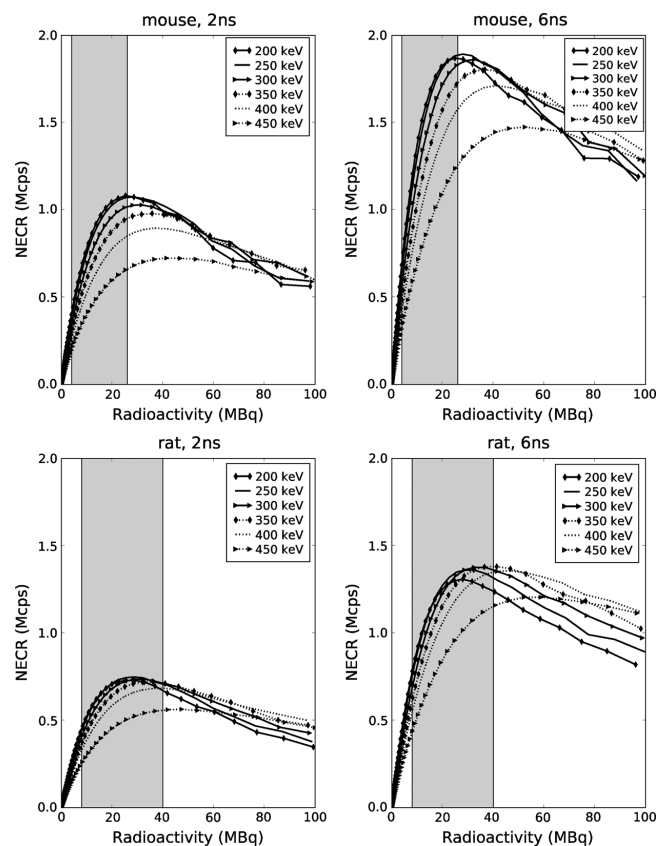


Fig. 5. NECR curves for the mouse- and rat-sized cylinders obtained for various CWs and EWs. The results are derived from the count-rate measurements shown in Fig. 4 and the vertical bars indicate the typical ranges of radioactivity used in FDG-PET imaging of mice and rats.

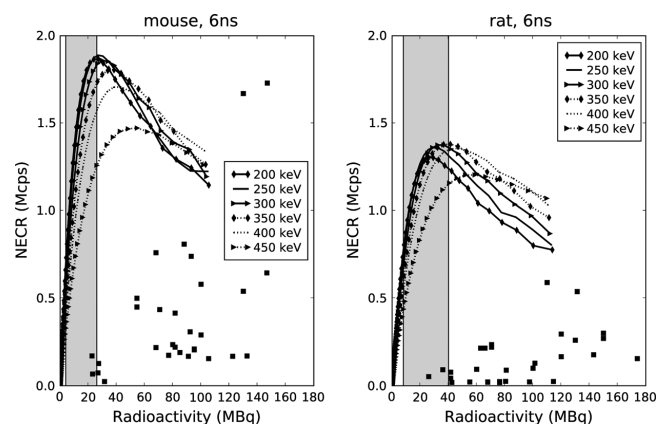


Fig. 6. NECR curves of the prototype, obtained by using a 6 ns CW and various EWs, along with the NECR peaks (squares) reported in the literature for other  $\mu$ PET systems [3], [4], [11], [13], [40]–[56]. The vertical bars show the typical ranges of radioactivity currently employed in FDG-PET imaging of mice and rats. These results must be interpreted with great caution (see text).

of scatter accounted for. Fig. 7 shows the NES estimated for our prototype, obtained by fitting the low-activity regions of the NECR curves with least-square lines to reduce the effects of noise to the estimation of the slopes. Our results show that the NES values can reach 26.4% and 22.2% for the mouse- and rat-sized cylinders, respectively, when using a 250–750 keV EW

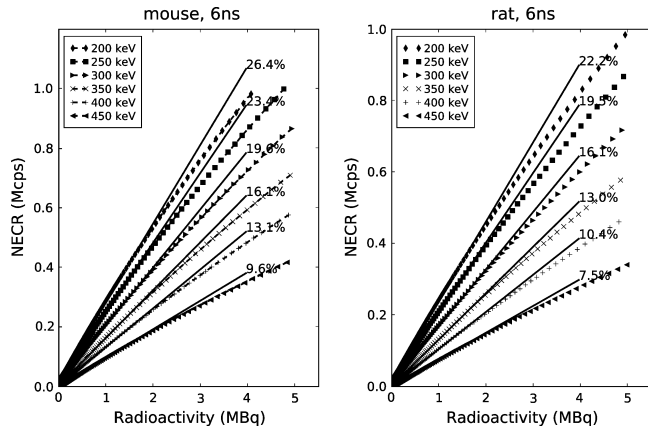


Fig. 7. NES of the prototype, obtained by using a 6 ns CW and various EWs. Symbols show the measured NECR curves obtained with various LLD settings for the EW (the ULD equals 750 keV) and the solid lines are their least-square fitting lines at low radioactivities. The slopes of these lines, i.e., the NES values, are indicated.

and 6 ns CW. When using a 450–750 EW, the NES values remain high at 9.6% and 7.5% for the mouse- and rat-sized cylinders, respectively.

The NECR and NES considered above do not account for the negative impact of the background event rates due to Lu-176 in LSO and LYSO to the system sensitivity. In principle, the Lu-176 background event rates can be treated similarly as scatter and random rates are treated by the definition of NECR (and NES). Here, we note the following. At the zero activity, eq. (1) becomes  $NECR = (1 - SF) \times P_0$ , where  $P_0$  is the Lu-176 background event rates. Therefore,  $P_0$  can be assessed by the intercepts of the curves shown in Fig. 7 at zero radioactivity. Evidently, the Lu-176 background event rates of the prototype are low with respect to the event rates measured at the typical ranges of radioactivity used in FDG-PET rodent imaging. Therefore, they will not affect the NECR and NES values obtained at these ranges. However, at very low radioactivity, e.g.,  $<0.5$  MBq ( $13.5 \mu\text{Ci}$ ), because the negative impact of the Lu-176 background event rates to sensitivity is ignored the reported NECR and NES values will over-estimate the net sensitivity of the prototype.

### C. DOI Blurring

As already mentioned above, we expect the prototype to exhibit substantial DOI blurring. To demonstrate, Fig. 8 shows the sensitivity functions of selected LORs on the midplane between the two detectors of the prototype, obtained by using MC simulation. The long axes of these sensitivity functions reflect the directions of the LORs projected onto the midplane. It is evident that the sensitivity function grows wider for more oblique LORs. Specifically, the sensitivity function of the vertical LOR is isotropic and has an FWHM of 1.2 mm. In contrast, the sensitivity function of the most oblique LOR shown has a 1.4 mm FWHM along its short axis and an 8.0 mm FWHM along its long axis.

We have performed some initial measurements toward validating the spatial response functions generated by MC simulation. We employed a spinal needle having an external

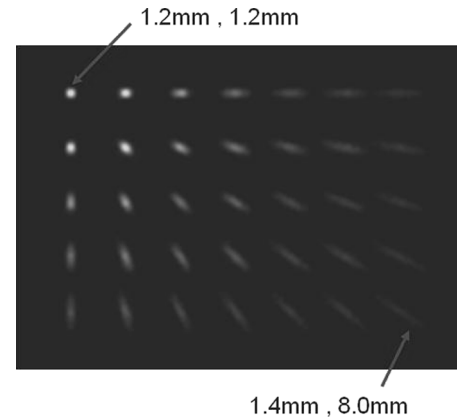


Fig. 8. Images showing sample sensitivity functions of 35 LORs of the prototype on the midplane between the two detectors of the prototype. The long axes of these sensitivity functions reflect the directions of the LORs projected onto the midplane. The upper-left sensitivity function is associated with an LOR that is vertical to the detectors. It is isotropic and has an FWHM of 1.2 mm. The lower-right sensitivity function is associated with the most oblique LOR of the 35 LORs examined. Its short axis has a 1.4 mm FWHM and its long axis has an 8.0 mm FWHM. These sensitivity functions demonstrate that substantial DOI blurring is present.

diameter of  $\sim 0.74$  mm; filled it with FDG; and placed it parallel to the detectors of the prototype. We first obtained reconstructed images of the spinal needle without correcting for the DOI blurring and extracted the axis of the needle from the resulting images. Then, fan-beam projection images of the needle were calculated by using the derived location of the axis and estimated response functions of the prototype. The response functions were estimated either by using MC simulation (which modeled the effects of finite detector size and DOI blurring) or by using a raytracing technique (which assumed the ideal line-integral projection model and hence ignored the effects of finite detector size and DOI blurring). The finite diameter of the spinal needle was neglected in these computations. Fig. 9 compares several measured profiles with their estimated profiles obtained for the spinal needle by using the procedure describe above. The results show significant differences between the calculated profiles obtained by using the raytracing-generated response functions with the measurements, reflecting the presence of substantial resolution degradations in the prototype. In comparison, the calculated profiles obtained by using the MC-generated response functions provide better agreement to the measurements.

Although the MC-generated response functions are more accurate than the raytracing-generated response functions, more detailed and comprehensive quality assessment of the former is needed because the quality of the images generated by the prototype is strongly dependent upon the accuracy of these response functions. We will address this important task in future studies.

### D. Resolution Phantom

The spatial resolution of the prototype was evaluated by using a resolution phantom (Ultra-Micro Hot Spot phantom, Data Spectrum Corporation) that consisted of rod sources of various diameters, ranging from 0.75 mm to 2.4 mm. The phantom was filled with  $\sim 2.6$  MBq ( $\sim 70 \mu\text{Ci}$ ) FDG, placed with its axis vertical to the HRRT detectors, and scanned for two hours. The data were corrected for randoms (by subtracting the delayed

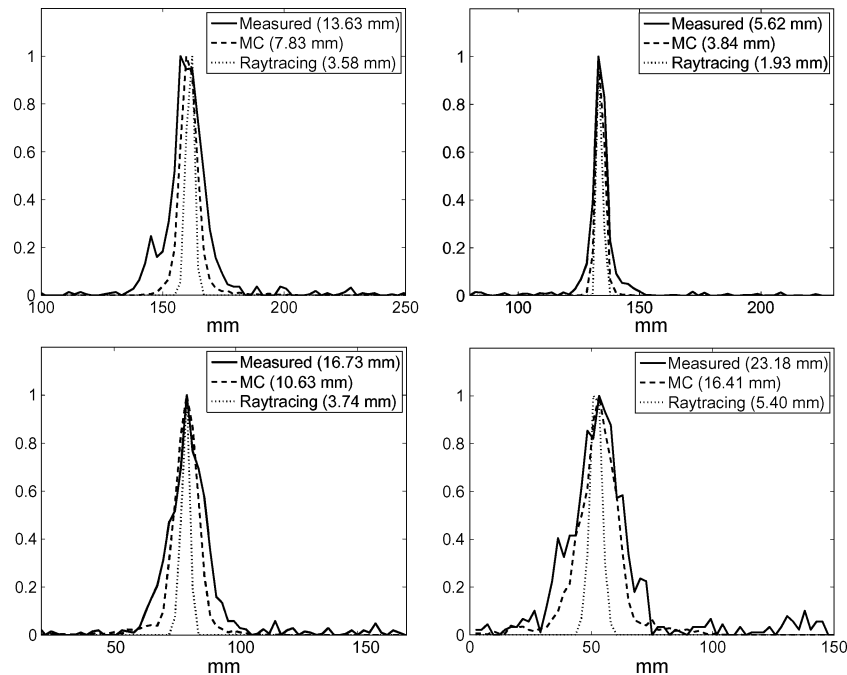


Fig. 9. Sample intensity profiles of the measured projection images of a spinal needle filled with FDG, in comparison with the predicted profiles obtained by using spatial response functions calculated for the prototype. In these plots, the profiles are scaled to have a maximum value of 1.0, the unit of the horizontal axes is millimeter (mm), and the numbers in parentheses are the FWHMs of the profiles. The spatial response functions were computed either by using MC simulation that included the effects of finite detector size and DOI blurring, or by using a raytracing technique that assumed the ideal line-integral projection model. The MC-generated response functions provide better agreement to the measurements than the raytracing-generated response functions. Note that the spinal needle has an external diameter of  $\sim 0.74$  mm; this diameter was not included in calculating the profiles.

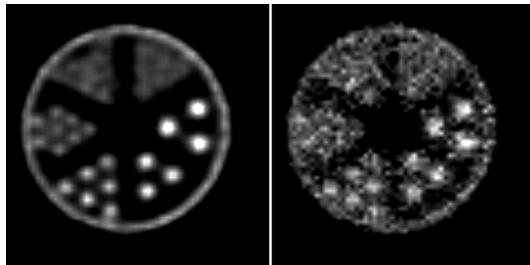


Fig. 10. Cross-sectional images of a resolution phantom (Ultra-Micro Hot Spot phantom, Data Spectrum Corporation) obtained by applying two iterations of an OSEM algorithm, which employs MC- (left) or raytracing-generated (right) response functions, to the same measured dataset. The phantom contains six groups of rods having diameters of 2.4 mm, 2.0 mm, 1.70 mm, 1.35 mm, 1.0 mm and 0.75 mm. The spacing between two neighboring rods in the same group is twice their diameter. The data were corrected for randoms, but not for attenuation or scatter. The MC image has better resolution and statistics, clearly resolving the 1.35 mm rods. By fitting with Gaussian functions, these rods have an average FWHM of 1.79 mm.

events) and normalized, but no scatter or attenuation correction was performed. The left image in Fig. 10 shows the resulting image (reconstructed by using MC-generated response functions). Evidently, the 1.35 mm rods are resolved. By fitting their intensity profiles with Gaussian functions, the 1.35 mm rods have an FWHM ranging from 1.55 mm to 1.92 mm and an average FWHM of 1.79 mm. For providing a crude estimate for the system resolution, we applied the quadrature rule  $r_i^2 = r_o^2 + r_s^2$ , where  $r_i$ ,  $r_o$ , and  $r_s$  are the image, object, and system resolutions in FWHM, to the average FWHM and obtained a resolution of  $\sim 1.18$  mm FWHM for the prototype. This is consistent with the  $\sim 1.2$  mm resolution that we have previously estimated by using simulation data [32]–[34].

To demonstrate the important role of model-based image reconstruction in the design of the prototype, Fig. 10 (right image) also shows the image of the resolution phantom obtained by using the raytracing-generated response functions. In comparison with the MC result, the image is much noisier and much limited in resolution.

#### E. Real-Data Rat Images

We have also employed our prototype for imaging rodents (using the MC-generated response functions in reconstruction). Fig. 11 shows sample cross-sectional images and a maximum-intensity projection (MIP) image obtained for a 270 g healthy rat from a 30-minute dataset acquired at  $\sim 40$  minutes post  $\sim 18.5$  MBq ( $\sim 500 \mu\text{Ci}$ ) FDG bolus injection. The rat was positioned such that: the HRRT detectors were above and below the rat; the long sides of the HRRT detectors (i.e., the 25 cm sides) were parallel to the length of the rat; and the rat's brain was at the center of the prototype (therefore, the coronal and sagittal views in Fig. 11 show only half of the scanner's AFOV). The EW and CW used were 450–650 keV and 6 ns, respectively. Randoms correction was achieved by subtracting the delayed events from the prompt events. Again, no scatter or attenuation correction was applied. In these images, the heart of the rat is resolved. Fig. 12 similarly shows the results obtained from a 1-minute subset extracted from the end of this 30-minute dataset. While considerable noise is observed, this 1-minute dataset (which is obtained at  $\sim 70$  minutes post injection) can still generate images that resolve the heart. We note that no significant image artifacts are observed even though the data are theoretically incomplete (see Appendix).

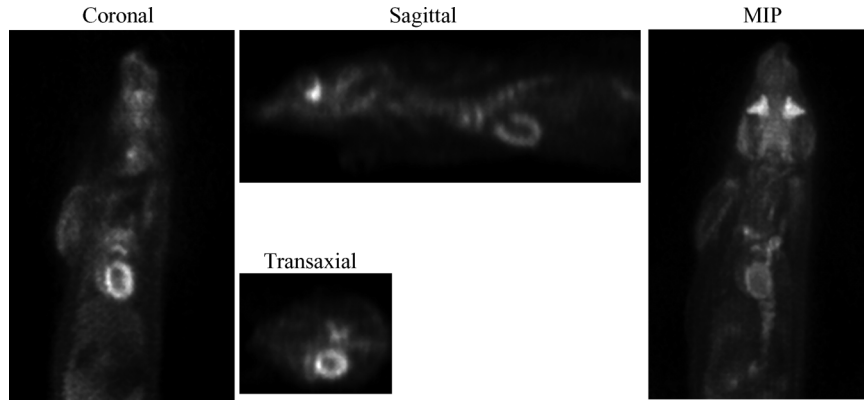


Fig. 11. Selected cross-sectional images and a maximum-intensity-projection (MIP) image obtained for a 270 g healthy rat from a 30-minute dataset acquired at  $\sim 40$  minutes after a bolus injection of  $\sim 18.5$  MBq ( $\sim 500 \mu\text{Ci}$ ) FDG. Randoms are corrected for by subtracting the delayed events from the prompt events. Scatter and subject attenuation are not corrected for.

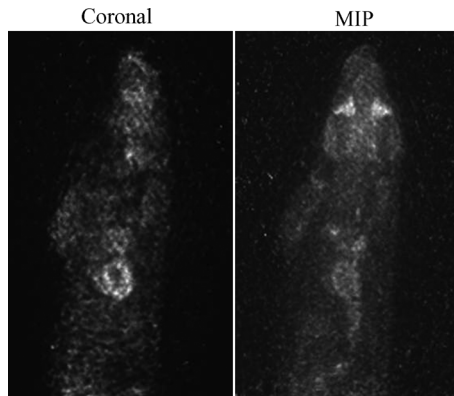


Fig. 12. A sample cross-sectional image and an MIP image obtained from a 1-minute dataset extracted from the end of the dataset that generates the images shown in Fig. 11.

## V. CONCLUSIONS AND DISCUSSION

By adopting the integrative design strategy, we have developed a compact, dual-head  $\mu\text{PET}$  prototype scanner that can achieve a central sensitivity of  $\sim 30\%$ . By using a resolution phantom with its axis placed vertical to the detectors of the prototype, we also show that an average FWHM of 1.79 mm can be obtained for 1.35 mm-diameter rod sources, which is consistent with the 1.2 mm FWHM resolution that we have previously estimated by using simulation data. The prototype is stationary and has a large FOV that allows for whole-body imaging of an entire rodent (or even multiple rodents) at a single bed position. The combination of high sensitivity and large FOV makes the prototype useful for monitoring the spatio-temporal distributions of radiotracers at high temporal resolutions and over long periods of time inside the entire subject. Over the typical ranges of radioactivity currently been used for FDG-PET rodent imaging, the NECR of the prototype are considerably higher than those of other  $\mu\text{PET}$  systems. NES values of 26.4% and 22.2% can be obtained for mouse- and rat-sized cylinders.

Because the HRRT detectors are not specifically designed for implementing HS  $\mu\text{PET}$  systems of concern in this paper, the count-rate capability of the prototype scanner is somewhat limited. For purpose of demonstration, Fig. 13 compares the NECR curves measured for the prototype with those obtained by Monte

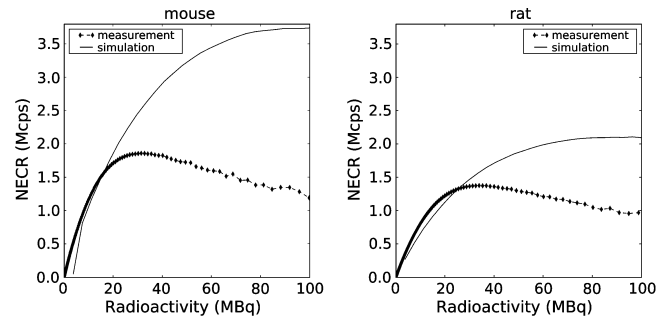


Fig. 13. Measured and simulated NECR curves for the mouse- and rat-sized cylinders obtained for the prototype when using a 6 ns CW and a 350–750 keV EW. In simulation, 20% energy resolution and 3 ns coincidence timing resolution are assumed.

Carlo (MC) simulation. Comparison of the results indicates that, due to the dead-time effect the measured NECR values are much lower than the simulation results at radioactivity above  $\sim 20$  MBq for both rat- and mouse-sized objects. However, this is a limitation due to a particular choice of the detector technology, not an intrinsic limitation of the design strategy.<sup>2</sup> We also note that if the CWs and EWs are properly selected our prototype is not critically count-rate limited over the typical ranges of radioactivity currently being used for FDG rodent imaging (cf. Figs. 5 and 6).

It is important to note that the above-mentioned “typical” ranges of radioactivity are determined for existing  $\mu\text{PET}$  systems. Our prototype is considerably more sensitive and hence lower radioactivities can be used, further alleviating the concern for the limited count-rate performance of the prototype in practical use. However, at sufficiently low radioactivity (e.g., below 0.5 MBq) the background event rates due to Lu-176 in LSO and LYSO can substantially diminish the net sensitivity of the prototype. Therefore, the prototype may not be optimal for imaging studies that employ very low radioactivity. We will investigate this issue in future studies.

<sup>2</sup>Therefore, the count-rate performance of our prototype is far from what its hardware configuration can potentially achieve when faster electronics are employed. We note that there are also other limitations to the HRRT detectors. For example, there is a high-level multiplexing on the PMTs, which will complicate the dead-time behavior of the system.



The results shown in Fig. 9 indicate that the response functions currently used in our model-based reconstruction algorithm can be made more accurate to yield images having better resolution than reported in this paper. Therefore, the performance characteristics of our prototype still have much room for improvement. Although its design remains to be optimized, the performance properties of the prototype have nonetheless presented supporting evidence to the usefulness of the integrative design strategy for developing HS  $\mu$ PET systems. In particular, we show the integrative design strategy can substantially relax the performance requirements for the hardware components with respect to the target system performance. As a result, we are able to employ the mature HRRT detector technology for developing an HS  $\mu$ PET scanner immediately, rather than waiting for more advanced detector technologies to become available.

It needs to be emphasized that the contribution of this paper is the development of an HS  $\mu$ PET system by adopting the integrative design strategy, rather than advocating a specific detector technology and scanner geometry for developing  $\mu$ PET systems. Therefore, the work presented in this paper shall not be taken to mean that the HRRT detectors and the dual-head geometry are more favorable than other detectors and scanner geometries for building HS  $\mu$ PET systems. The relative advantages and shortcomings of various detector technologies and scanner geometries for implementing HS  $\mu$ PET systems, adopting the integrative design strategy or not, is an important question that deserves future research attention. Also, the concept of achieving integrative designs for PET systems does not diminish the fundamental significance of detector technology research.

Finally, we note that little quantitative information is currently available to guide the integrative design strategy. Therefore, as illustrated by our discussion in Section III and Appendix, the design of our prototype is based largely on qualitative observations rather than on quantitative principles. To develop such principles, one needs to have the ability to quantitatively predict various properties of the resulting images when given the hardware and software features of the system, the achievable accuracy in modeling the physical and statistical responses of the system, and the expected imaging conditions (e.g., subject size, isotope and radioactivity, and scan time). Fessler *et al.* [57] and Qi *et al.* [58], [59] have developed theoretical methods that can provide such ability for some iterative reconstruction methods. In future studies, we will investigate the application and extension of these methods for developing the theoretical frameworks to more firmly establish the integrative design strategy.

#### APPENDIX

Below, we discuss several important integrative design considerations for the prototype that are omitted in Section III to avoid distracting the readers' attention from the main ideas behind the design of the prototype.

First, we note that increasing the GE does not necessarily improve the net sensitivity of a PET scanner because scatter and randoms can increase at even faster rates [38], [39]. Fortunately, this concern for elevated scatter and randoms is greatly alleviated in  $\mu$ PET imaging by the very nature of the imaging task:

the subject is small (thus reduced scatter) and the amount of radiotracer administered is low (thus reduced randoms). Therefore, we believe that in  $\mu$ PET imaging increasing the GE (by use of compact geometry) is an effective way for increasing the net sensitivity if adequate EWs and CWs are used. Our NECR and NES results confirm this stipulation.

Second, we note that the stationary, dual-head geometry of the prototype cannot completely surround the subject and will produce theoretically incomplete data. Despite this, we are interested in the stationary geometry for the following reasons. First, the mechanical design is simple and there is no need for maintaining the mechanical alignment during motion. Second, motion introduces additional complexity in reconstruction and can decrease the image temporal resolution. Third, with the compact, dual-head geometry subject handling is easier, and the entire volume between the detectors can be used for imaging, when the scanner stays stationary.<sup>3</sup> While not eliminating it, we note that the use of compact geometry can considerably reduce data incompleteness. Therefore, we stipulate that data incompleteness of the prototype will not present a critical challenge to image reconstruction. This stipulation is supported by our simulation and real-data results.

The third consideration concerns the selection for the target image resolution. In theory, one can rely on the image reconstruction process to perform aggressive corrections for the DOI blurring and other resolution degradations, while eliminating altogether the use of DOI detectors, for achieving high image resolution. At issue with this software-based approach is the amplification of data noise, modeling errors and computation errors in any resolution-recovery process. By performing aggressive corrections, the benefits provided by the gained sensitivity can be lost to the substantially amplified noise and errors in image. Furthermore, to perform aggressive corrections one must have an accurate model of the physical and statistical properties of the detection responses of the imaging system. However, only limited accuracy can be achieved in practice. On the other hand, a system can also rely solely on its hardware features for meeting its performance targets. When adopting this hardware-based approach, as we have noted in Section II, adequate detector technologies may not be available or available technologies may be too costly. When adopting the integrative design strategy, one therefore must take care to create a system design in which the resolution degradations presented by the hardware features of the system (using existing and affordable detector technologies) with respect to the performance targets of the system can be effectively corrected for by the software features of the system. Hence, we use thick detectors having moderate DOI resolution to provide high system sensitivity but avoid creating too strong DOI blurring to correct for with the compact geometry of the prototype. Also, we pick the intrinsic detector resolution for the target system resolution to limit the degree of resolution correction that is needed. Our initial result with the resolution phantom suggests that the target resolution is adequate. However, more concrete quantitative principles are needed to guide the integrative design strategies.

<sup>3</sup>When employing detector motion, only the central cylindrical volume having a diameter equal to the detector spacing can be used for imaging. Furthermore, most LORs will not pass through this cylindrical volume, resulting in extremely poor utilization of the detection channels.

## ACKNOWLEDGMENT

The authors thank Dr. Bill C. Penney for making FDG available, to Drs. Bill C. Penney, Yonling Pu and Carl Valentin for conducting the FDG rat imaging study, and to the Siemens Medical Solutions, Inc. for providing the HRRT detectors.

## REFERENCES

- [1] S. Cherry, "Fundamentals of positron emission tomography and applications in preclinical drug development," *J. Clin. Pharmacol.*, vol. 41, pp. 482–491, 2001.
- [2] R. J. Walledge, R. Manavaki, A. J. Reader, A. P. Jeavons, P. J. Julian, and S. Zhao *et al.*, "Quad-HIDAC PET: Comparison of four image reconstruction techniques high resolution imaging," in *IEEE Nuclear Science Symposium and Medical Imaging Conference Record*, 2001, pp. 1816–1820.
- [3] Y.-C. Tai, A. F. Chatzioannou, Y. Yang, R. W. Silverman, K. Meadors, and S. Siegel *et al.*, "MicroPET II: Design, development and initial performance of an improved microPET scanner for small-animal imaging," *Phys. Med. Biol.*, vol. 48, no. 11, pp. 1519–1537, 2003.
- [4] Y. Yang, Y.-C. Tai, S. Siegel, D. F. Newport, B. Bai, and Q. Li *et al.*, "Optimization and performance evaluation of the microPET II scanner for *in vivo* small-animal imaging," *Phys. Med. and Biol.*, vol. 49, no. 12, pp. 2527–2545, 2004.
- [5] R. Lecomte, "Technology challenges in small animal PET imaging," *Nucl. Instr. and Meth. Phys. A*, vol. 527, pp. 157–165, 2004.
- [6] Y. Tai and R. Laforest, "Instrumentation aspects of animal PET," *Annu. Rev. Biomed. Eng.*, vol. 7, pp. 255–285, 2005.
- [7] A. F. Chatzioannou, "Molecular imaging of small animals with dedicated PET tomographs," *Eur. J. Nucl. Med.*, vol. 29, pp. 98–114, 2002.
- [8] S. Hume, R. Gunn, and T. Jones, "Pharmacological constraints associated with positron emission tomographic scanning of small laboratory animals," *Eur. J. Nucl. Med.*, vol. 25, pp. 173–176, 1998.
- [9] N. Adonai, K. Nguyen, J. Walsh, M. Iyer, T. Toyokuni, and M. Phelps *et al.*, "Ex vivo cell labeling with  $^{64}\text{Cu}$ -pyruvaldehyde-bis( $\text{N}^4$ -methylthiosemicarbazone) for imaging cell trafficking in mice with positron-emission tomography," *Proc. Natl. Acad. Sci. USA*, vol. 99, pp. 3030–3035, 2002.
- [10] T. Funk, S. Mingshan, and B. Hasegawa, "Radiation dose estimate in small animal SPECT and PET," *Med. Phys.*, vol. 31, pp. 2680–2686, 2004.
- [11] Q. Bao, D. Newport, M. Chen, D. B. Stout, and A. F. Chatzioannou, "Performance evaluation of the Inveon dedicated PET preclinical tomograph based on the NEMA NU-4 standards," *J. Nucl. Med.*, vol. 50, pp. 401–408, 2009.
- [12] C.-M. Kao and C.-T. Chen, "Development and evaluation of a dual-head PET system for high-throughput small-animal imaging," in *IEEE Nuclear Science Symposium and Medical Imaging Conference Record*, 2003, pp. M6–M29.
- [13] Y.-C. Tai, A. F. Chatzioannou, S. Siegel, J. Young, D. Newport, and R. N. Goble *et al.*, "Performance evaluation of the microPET P4: A PET system dedicated to animal imaging," *Phys. Med. Biol.*, vol. 46, pp. 1845–1862, 2001.
- [14] F. Habte, A. K. Foudray, P. Olcott, and C. Levin, "Effects of system geometry and other physical factors on photon sensitivity of high resolution positron emission tomography," *Phys. Med. Biol.*, vol. 52, pp. 3753–3772, 2007.
- [15] J. Karp and M. Daube-Witherspoon, "Depth-of-interaction determination in NaI(Tl) and BGO scintillation crystals using a temperature gradient," *Nucl. Instr. and Meth. A*, vol. 260, p. 509, 1987.
- [16] C. Carrier, C. Martel, D. Schmitt, and R. Lecomte, "Design of a high resolution positron emission tomograph using solid state scintillation detectors," *IEEE Trans. Nucl. Sci.*, vol. 35, pp. 685–690, 1988.
- [17] P. Bartzakos and C. Thompson, "A depth-encoded PET detector," *IEEE Trans. Nucl. Sci.*, vol. 38, pp. 732–738, 1991.
- [18] J. Rogers, C. Moisan, E. Hoskinson, M. Andreaco, C. Williams, and R. Nutt, "A practical block detector for a depth-encoding PET system," *IEEE Trans. Nucl. Sci.*, vol. 43, pp. 3240–3248, 1996.
- [19] M. Dahlbom, L. MacDonald, M. Schmand, L. Eriksson, M. Andreaco, and C. Williams, "A YSO/LSO phoswich array detector for single and coincidence photon imaging," *IEEE Trans. Nucl. Sci.*, vol. 45, pp. 1128–1132, 1998.
- [20] R. Miyaoka, T. Lewellen, and H. Yu, "Design of a depth of interaction (DOI) PET detector module," *IEEE Trans. Nucl. Sci.*, vol. 45, pp. 1069–1073, 1998.
- [21] C. Mosian, M. Andreaco, J. Rogers, S. Paquet, and D. Voza, "Segmented LSO crystals for depth-of-interaction encoding in PET," *IEEE Trans. Nucl. Sci.*, vol. 45, pp. 3030–3035, 1998.
- [22] M. Schmand, L. Eriksson, M. E. Casey, K. Wienhard, G. Flügge, and R. Nutt, "Advantages using pulse shape discrimination to archive the depth of interaction information (DOI) from a multi-layer phoswich detector," in *IEEE Nuclear Science Symposium and Medical Imaging Conference Record*, 1998, pp. 1095–1099.
- [23] S. McCallum, P. Clowes, and A. Welch, "A four-layer attenuation compensated PET detector based on APD arrays without discrete crystal elements," *Phys. Med. Biol.*, vol. 50, pp. 4187–4207, 2005.
- [24] N. Inadama, H. Murayama, Y. Ono, T. Tsuda, M. Hamamoto, and T. Yamaya *et al.*, "Performance evaluation for 120 four-layer DOI block detectors of the jPET-D4," *Radiol. Phys. Technol.*, vol. 1, pp. 75–82, 2008.
- [25] W.-H. Wong, J. Uribe, K. Hicks, and G. Hu, "A 2-dimensional detector decoding study on BGO arrays with quadrant sharing photomultipliers," *IEEE Trans. Nucl. Sci.*, vol. 41, pp. 1453–1457, 1994.
- [26] S. Surti and J. S. Karp, "Imaging characteristics of a 3-dimensional GSO whole-body PET camera," *J. Nucl. Med.*, vol. 45, pp. 1040–1049, 2004.
- [27] H. Baghaei, H. Li, J. Uribe, Y. Wang, and W.-H. Wong, "Compensation of missing projection data for MDAPET camera," in *IEEE Nuclear Science Symposium and Medical Imaging Conference Record*, 2000, pp. 17/41–17/45.
- [28] J. Zhang, P. Oclott, A. Foudray, G. Chinn, and C. Levin, "Study of count performance, lesion visualization, and contrast resolution as a function of crystal resolution for a dual-plate PET camera dedicate to breast cancer imaging," in *IEEE Nuclear Science Symposium and Medical Imaging Conference Record*, 2005, pp. 1667–1671.
- [29] S. Moehrs, A. Del Guerra, D. Herbert, and M. Mandelkern, "A detector head design for small-animal PET with silicon photomultipliers (SiPM)," *Phys. Med. Biol.*, vol. 51, pp. 1113–1127, 2006.
- [30] R. Leahy and J. Qi, "Statistical approaches in quantitative positron emission tomography," *Statistics and Computing*, vol. 10, pp. 147–165, 2000.
- [31] J. Qi and R. Leahy, "Iterative reconstruction techniques in emission computed tomography," *Phys. Med. Biol.*, vol. 51, pp. R541–R578, 2006.
- [32] C.-M. Kao and Y. Dong, "Image reconstruction of a dual-head small-animal PET system by using Monte Carlo computed system response matrix," in *Conference Record of the 9th Fully 3-D Image Reconstruction in Radiology and Nuclear Medicine*, 2007.
- [33] C.-M. Kao and Y. Dong, "Evaluation of fully 3-D image reconstruction methods for a dual-head small-animal PET scanner," in *IEEE Nuclear Science Symposium and Medical Imaging Conference Record*, 2007, pp. M13–M142.
- [34] C.-M. Kao, Y. Dong, Q. Xie, and C.-T. Chen, "Accurate image reconstruction with computed system response matrix for a high-sensitivity dual-head pet scanner," *IEEE Trans. Med. Imag.*, 2008, submitted for publication.
- [35] C. Michel, M. Schmand, X. Liu, M. Sibomana, S. Vollmar, and C. Knoss *et al.*, "Reconstruction strategies for the HRRT," in *IEEE Nuclear Science Symposium and Medical Imaging Conference Record*, 2000, pp. 15/207–15/212.
- [36] K. Wienhard, M. Schmand, M. E. Casey, K. Baker, J. Bao, and L. Eriksson *et al.*, "The ECAT HRRT: Performance and first clinical application of the new high resolution research tomograph," *IEEE Trans. Nucl. Sci.*, vol. 49, pp. 104–110, 2002.
- [37] H. de Jong, F. H. P. van Velden, R. W. Kloet, F. L. Buijs, R. Boellaard, and A. A. Lammertsma, "Performance evaluation of the ECAT HRRT: An LSO-LYSO double layer high resolution, high sensitivity scanner," *Phys. Med. Biol.*, vol. 52, pp. 1505–1526, 2007.
- [38] S. Cherry, J. Sorenson, and M. Phelps, *Physics in Nuclear Medicine*, 3rd ed. Philadelphia, PA: Elsevier Science, 2003.
- [39] M. Phelps, J. Mazziotta, and H. Schelbert, Eds., *Positron Emission Tomography and Autoradiography: Principles and Applications for the Brain and Heart*. New York: Raven Press, 1986.
- [40] S. Cherry, Y. Shao, R. Silverman, K. Meadors, S. Siegel, and A. Chatzioannou *et al.*, "MicroPET: A high resolution PET scanner for imaging small animals," *IEEE Trans. Nucl. Sci.*, vol. 44, pp. 1161–1165, 1997.
- [41] Y.-C. Tai, A. F. Chatzioannou, M. Dahlbom, and S. R. Cherry, "System design for a 1 mm<sup>3</sup> resolution animal PET scanner: MicroPET II," in *IEEE Nuclear Science Symposium and Medical Imaging Conference Record*, 2000, p. 21/52.

- [42] Y.-C. Tai, A. Chatziioannou, S. Siegel, J. Young, D. Newport, and R. N. Goble *et al.*, "Preliminary evaluation of the microPET P4: A PET system dedicated to small animal imaging," in *IEEE Nuclear Science Symposium and Medical Imaging Conference Record*, 2000, p. 21/51.
- [43] Y.-C. Tai, A. Ruangma, D. Rowland, S. Siegel, D. F. Newport, and P. L. Chow *et al.*, "Performance evaluation of the microPET focus: A third-generation microPET scanner dedicated to animal imaging," *J. Nucl. Med.*, vol. 46, pp. 455–463, 2005.
- [44] Y. Wang, J. Seidel, B. M. Tsui, J. J. Vaquero, and M. G. Pomper, "Performance evaluation of the GE healthcare eXplore VISTA dual-ring small-animal PET scanner," *J. Nucl. Med.*, vol. 47, pp. 1891–1900, 2006.
- [45] A. P. Jeavons, R. A. Chandler, and C. A. R. Dettmar, "A 3-D HIDACPET camera with sub-millimetre resolution for imaging small animals," *IEEE Trans. Nucl. Sci.*, vol. 46, pp. 468–473, 1999.
- [46] J. Missimer, Z. Masi, M. Honer, C. Keller, A. Schubiger, and S. Ametamey, "Performance evaluation of the 16-module quad-HIDAC small animal PET camera," *Phys. Med. Biol.*, vol. 49, pp. 2069–2081, 2004.
- [47] K. P. Schafers, A. J. Reader, M. Kriens, C. Knoess, O. Schober, and M. Schafers, "Performance evaluation of the 32-module quadHIDAC small-animal PET scanner," *J. Nucl. Med.*, vol. 46, pp. 996–1004, 2005.
- [48] N. C. Rouze, W. Winkle, and G. D. Hutchins, "IndyPET—A high resolution, high sensitivity dedicated research scanner," in *IEEE Nuclear Science Symposium and Medical Imaging Conference Record*, 1999, pp. 1460–1464.
- [49] K. Ziemons, E. Auffray, R. Barbier, G. Brandenburg, P. Bruyndonckx, and Y. Choi *et al.*, "The ClearPET project: Development of a 2nd generation high-performance small animal PET scanner," *Nucl. Instr. Meth. A*, vol. 537, pp. 307–311, 2005.
- [50] J. Seidel, J. Vaquero, and M. Green, "Resolution uniformity and sensitivity of the NIH ATLAS small animal PET scanner: Comparison to simulated LSO scanners without depth-of-interaction capability," *IEEE Trans. Nucl. Sci.*, vol. 50, pp. 1347–1350, 2003.
- [51] S. Surti, J. S. Karp, A. E. Perkins, R. Freifelder, and G. Muehllehner, "Design evaluation of A-PET: A high sensitivity animal PET camera," *IEEE Trans. Nucl. Sci.*, vol. 50, pp. 1357–1363, 2003.
- [52] A. D. Guerra, A. Bartoli, N. Belcari, D. Herbert, A. Motta, and A. Vaiano *et al.*, "Performance evaluation of the fully engineered Yap-(S)PET scanner for small animal imaging," *IEEE Trans. Nucl. Sci.*, vol. 53, pp. 1078–1083, 2006.
- [53] R. Laforest, D. Longford, S. Siegel, D. F. Newport, and J. Yap, "Performance evaluation of the microPET-Focus-F120," *IEEE Trans. Nucl. Sci.*, vol. 54, pp. 42–49, 2007.
- [54] D. P. McElroy, W. Pimpl, B. J. Pichler, M. Rafecas, T. Schuler, and S. I. Ziegler, "Characterization and readout of MADPET-II detector modules: Validation of a unique design concept for high resolution small animal PET," *IEEE Trans. Nucl. Sci.*, vol. 52, pp. 199–204, 2005.
- [55] M. Rafecas, B. Mosler, M. Dietz, M. Pogl, A. Stamatakis, and D. P. McElroy *et al.*, "Use of a Monte Carlo-based probability matrix for 3-D iterative reconstruction of MADPET-II data," *IEEE Trans. Nucl. Sci.*, vol. 51, pp. 2597–2605, 2004.
- [56] C. C. Constantinescu and J. Mukherjee, "Performance evaluation of an Inveon PET preclinical scanner," *Phys. Med. Biol.*, vol. 54, pp. 2885–2899, 2009.
- [57] J. A. Fessler and W. L. Rogers, "Spatial resolution properties of penalized-likelihood image reconstruction: Space-invariant tomographs," *IEEE Trans. Image Proc.*, vol. 9, pp. 1346–1358, 1996.
- [58] J. Qi and R. M. Leahy, "A theoretical study of the contrast recovery and variance of MAP reconstructions from PET data," *IEEE Trans. Med. Imag.*, vol. 18, pp. 293–305, 1999.
- [59] J. Qi and R. M. Leahy, "Resolution and noise properties of MAP reconstruction for fully 3-D PET," *IEEE Trans. Med. Imag.*, vol. 19, pp. 493–506, 2000.